# Chapter 6
Piezotronic Electromechanical Memories

Abstract In this chapter, we treat the piezoelectrically modulated resistive switching device based on a piezotronic nanowire, through which the write/read access of the memory cell is programmed via electromechanical modulation. Adjusted by the strain-induced polarization charges created at the semiconductor/metal interface under externally applied deformation by the piezoelectric effect, the resistive switching characteristics of the cell can be modulated in a controlled manner, and the logic levels of the strain stored in the cell can be recorded and read out, which has the potential for integrating with NEMS technology to achieve micro/nanosystems capable for intelligent and self-sufficient multidimensional operations.

The concept of complementing field effect transistors (FETs) with two-terminal hysteretic resistive switches has recently attracted great interest in implementing and scaling novel non-volatile resistive memories [1–5] for ultrahigh-density memory storage [6, 7] and logic applications [8, 9] with characteristics such as high density, low cost, fast write/read accessing speed and long endurance/retention time [10]. Notably, previously existing non-volatile resistive memories are all based on electrically switchable resistance change [10] by means of formation of conductive filaments [5, 11], charge-transfer-induced conformational change [12], electrochemical processes [13], or field-assisted drift/diffusion of charged ions [3, 4, 6, 14] in various oxides and ionic conductors [15, 16]. These devices are electrically programmed and they are not suitable for direct interfacing with actuation/triggering other than electrical input.

For applications such as human–computer interfacing, sensing/actuating in nanorobotics, and smart MEMS/NEMS [18], a direct interfacing of electronics with mechanical actions is required. In this chapter, we present the first piezoelectrically modulated resistive switching device based on piezotronic ZnO nanowire (NW), through which the write/read access of the memory cell is programmed via electromechanical modulation [17]. Adjusted by the strain-induced polarization charges created at the semiconductor/metal interface under externally applied deformation by the piezoelectric effect, the resistive switching characteristics of the cell can be modulated in a controlled manner, and the logic levels of the strain stored in the cell can be recorded and read out, which has the potential for integrating with NEMS
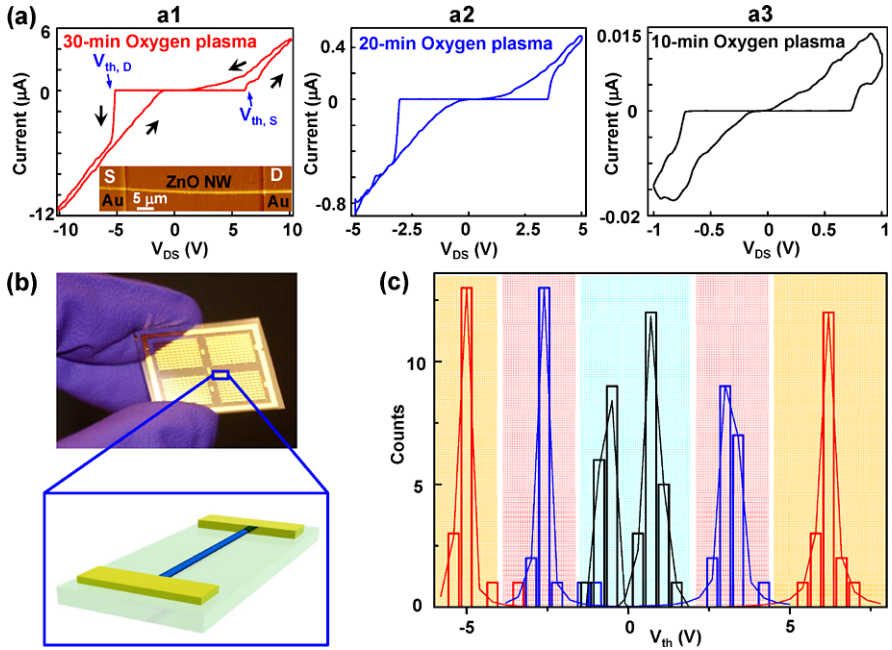
Fig. 6.1 Effects of oxygen–plasma treatment on electrical properties of ZnO PRM cells. (**a1**)–(**a3**) I–V characteristics of ZnO PRM cells after 30, 20 and 10 minutes oxygen–plasma treatment. The sweeping frequency is 0.1 Hz. (**a1**) *Inset*: Atomic force microscopy (AFM) image of one ZnO PRM cell. (**b**) Optical image of the large-scale as-fabricated PRM cells after printing transfer of ZnO NWs and lithography patterning of metal electrodes. (**c**) Statistical distributions of the $V_{th,S}$ and $V_{th,D}$ peaks for PRM cells with different periods of oxygen–plasma treatment. *Red*, *blue*, and *black lines* are for PRM cells with 30, 20, and 10 minutes oxygen–plasma treatment, respectively [17]

technology to achieve micro/nanosystems capable for intelligent and self-sufficient multidimensional operations [18, 20].

6.1 Device Fabrication

The basic structure of the piezoelectrically modulated resistive memory (PRM) is shown in Fig. 6.1(a1) (Inset), which consists of a ZnO piezotronic NW that is in contact with Au electrodes fabricated by lithography on a flexible PET substrate (from DuPont, thickness $\sim$ 1.25 mm). The two electrodes are labeled as the drain (D) and source (S) electrodes of the PRM cell. The single-crystalline ZnO NWs used in PRM devices were synthesized via a physical vapor deposition process [21] with diameters of 500 nm and lengths of 50 μm (Fig. 6.1(a1) (Inset)). ZnO NWs grown on alumina plates were transferred to the PET receiving substrate by sweeping the PET substrate across the NWs. Electrode patterns over the transferred ZnO NWs were

Fig. 6.2 $I-V$ curves of PRM cells with argon–plasma treatment. For PRM cells treated with argon plasma, the threshold voltages decreased and the conductance increased with respect to the pristine one, as the treatment time increased. The rectification disappeared in the $I-V$ curve for PRM cell treated with 30 minute argon plasma. *Inset*: magnified plot for pristine PRM cell and cell with 10-minute argon–plasma treatment [17]
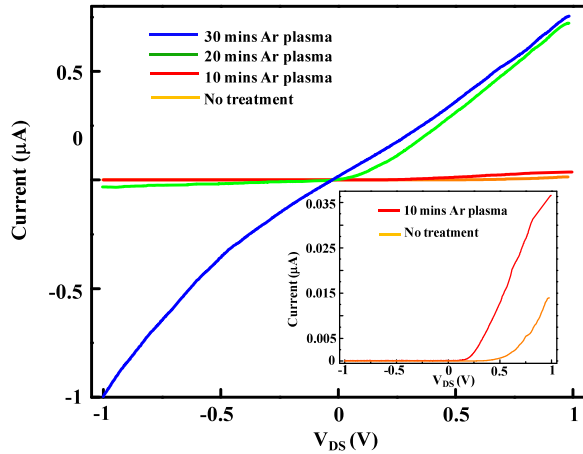
defined using photolithography and then followed by evaporating 350 nm thick Au film (E-beam evaporation). After lift-off step, a substantial amount of the ZnO NWs was patterned with ordered Au electrodes (Fig. 6.2). Au electrodes form Schottky contacts with the ZnO NWs, which are critical for a working piezotronic device. Finally, the entire substrate can be further packaged with a thin layer of PDMS to enhance mechanical robustness.

The PRM cells were then treated in oxygen plasma for 30 minutes before further characterization. Plasma treatment using argon or oxygen gas was performed on a plasma cleaning system (South Bay Technology, Inc., PC-150) in order to investigate the effect of pre-treatment on the performance and consequently the underlying working mechanism of the PRM cell. For both the argon– and oxygen–plasma treatment, the chamber pressure was maintained at 170 mTorr during the process. The forward power used was 30 W with the reflected power of 0 W. The duration time of plasma treatment was programmed to be from 10 to 30 minutes for different groups of PRM cells investigated.

6.2 Principle of Electromechanical Memory

Once the substrate is deformed, a pure tensile/compressive strain is created in the NW since the mechanical behavior of the entire cell structure is determined by the substrate (Fig. 6.1(b)). All of the $I-V$ curves presented were measured at a sweeping frequency of 0.1 Hz at room temperature unless otherwise noted. Several key features can be observed from the representative hysteretic $I-V$ curve obtained (Methods) for a single ZnO PRM cell (treated with 30-minute oxygen plasma) without applying an external strain (Fig. 6.1(a1)). First, as the bias voltage increased from 0 to 10 V, the output current of the PRM cell increased abruptly at 5.73 V, which is defined as the threshold point $V_{th,S}$. An abrupt transition and switching from high-resistance state (HRS) to low-resistance state (LRS) occurred at $V_{th,S}$. Secondly,

as the voltage was subsequently decreased towards negative values, the PRM cell switched back to the high-resistance OFF state. Thirdly, when the bias voltage exceeded certain negative values ($V_{th,D} = -5$ V in Fig. 6.1(a1), the PRM cell was turned to the ON state again and subsequent decrease in magnitude of the negative bias voltage switched the PRM cell back to the OFF state. This hysteretic sweeping sequence is indicated by arrowheads in Fig. 6.1(a1). The overall resistive switching observed for a single PRM cell is unipolar since the switching sequence is independent of the polarity of the bias voltage [10] (Fig. 6.1(a1)), which can be understood by the symmetry in structures of the PRM cells. Current rectification, which can minimize cross talk between individual memory cells and solve the sneak path problem in potential large-scale ultrahigh-density applications [22, 23], was also observed, suggesting that the PRM cell can be modeled as two back-to-back Schottky barriers connected in series with the NW in the metal–semiconductor–metal (M–S–M) configuration and the LRS state of the cell is dictated by Schottky-like transport at one of the Au/ZnO interfaces, which will be discussed in detail later.

Noticeably, the $I-V$ characteristic of the PRM cell is significantly different from those observed in previous single ZnO NW-based piezotronic devices [17, 18] (orange line in Fig. 6.2), which is proposed to result from the oxygen–plasma treatment prior to the measurement, as elaborated in the following. In order to investigate the effect of pre-treatment on the performance of the PRM cell, six groups of PRM cells were electrically characterized after different plasma pre-treatments (Methods). The first three groups were treated with oxygen plasma for 30, 20 and 10 minutes, respectively and the typical $I-V$ curves are shown in Figs. 6.1(a1)–(a3). The rest three groups of PRM cells were treated with argon plasma for 30, 20, and 10 minutes and their individual typical $I-V$ curves are shown in Fig. 6.2, respectively. The $I-V$ curve of the PRM cell directly assembled without pre-treatment (pristine PRM cell) is also plotted in Fig. 6.2 for comparison. It can be seen clearly that significant changes occur in the shape, threshold voltage, and current range of the $I-V$ curves for these samples. With increasing the period of time of treatment with oxygen plasma, the threshold voltage of the PRM cell increased accordingly, and increased hysteresis was also observed in the $I-V$ curve (Figs. 6.1(a1)–(a3)). If the PRM cell was treated with argon plasma, the threshold voltage decreased and the conductance increased with respect to the pristine one, and finally the rectification disappeared in the $I-V$ curve. The observed variations in the $I-V$ curves of the PRM cells, which were fabricated using the ZnO NWs synthesized under the same experimental condition, are due to the fact that oxygen vacancies are capable of influencing the Schottky contacts between ZnO and metal electrodes [24]. The synthesis condition (argon atmosphere at high temperature [21]) for ZnO NWs used in the reported piezotronic devices [26, 32] and pristine PRM cells tended to create a large amount of oxygen vacancies in the ZnO NWs, which possibly induced the observed lower threshold voltages of 0.5–0.7 V due to the high density of oxygen vacancies near the metal-ZnO interface and pinning of the ZnO Fermi level close to the $V_O^{\bullet\bullet}$ defect level [24]. If, however, the pristine ZnO NWs were treated with additional oxygen plasma for a prolonged period of time, the concentration of oxygen vacancies could be largely reduced, which contributed to the observed increase

in threshold voltages as well as the hysteresis loop of the $I-V$ curves, as shown in Figs. 6.1(a1)–(a3).

The mechanical deformations were applied onto the PRM cells using a 3-axis linear stage (Newport, Inc., 460P-XYZ-05). Electrical measurements were carried out with a computer-controlled data acquisition system, which consists of a function generator (Stanford Research Systems, Inc., DS345), a low-noise current preamplifier (Stanford Research Systems, Inc., SR570) and a shielded connector block with signal-labeled BNC connectors (NI BNC2120). For each strain state of the PRM cell, the output current was obtained by sweeping the DC bias across the device at a fixed frequency of 0.1 Hz.

The capability in designing the switching characteristics of the PRM cell in a controllable manner is further confirmed by the sharp and distinct statistical distributions of the $V_{th,S}$ and $V_{th,D}$ peaks for PRM cells with different periods of oxygen–plasma treatment, with $V_{th,S} = 6.15 \pm 0.39$ V and $V_{th,D} = -5.12 \pm 0.03$ V, $V_{th,S} = 3.18 \pm 0.20$ V and $V_{th,D} = -2.67 \pm 0.22$ V as well as $V_{th,S} = 0.74 \pm 0.51$ V and $V_{th,D} = -0.68 \pm 0.20$ V for PRM cells with treatment for 30, 20 and 10 minutes, respectively, by oxygen plasma (Fig. 6.1(c)). The predictable electrical properties of these ZnO NWs with controlled treatment process enable the reproducible assembly of NW structures at large quantity for further applications. The slight difference and asymmetry observed between $V_{th,S}$ and $V_{th,D}$ within each group of PRM cells is possibly induced by the non-uniform geometry of the ZnO NW, as indicated by the AFM image inset in Fig. 6.1(a1). It is well known that the Schottky barrier height (SBH) induced at a metal/semiconductor interface can be affected by factors such as the geometry and effective areas of the contact [25]. Moreover, the interface/surface states can also shift the SBH [25]. Notably, as can be seen from the semi-logarithmic plots of the data presented in Figs. 6.1(a1)–(a3) (Fig. 6.3), the PRM cells gradually lose their non-volatility as the period of oxygen–plasma treatment increases. The non-volatility of PRM cells with 10-minute oxygen–plasma treatment can be observed by sweeping only at positive voltages (0–1 V) and the high-conductance state is not lost at small bias in subsequent sweeps (for 20 cycles), which indicates that this kind of cell has the memory effect. The PRM cells with 30-minute oxygen plasma, however, did not show the same non-volatility in the current experiment.

6.3 Effect of Temperature on Memory Performance

Temperature-dependent $I-V$ measurements (Methods) were performed to obtain further insight into the switching mechanism of the PRM cell without applying external deformations. The representative result acquired from an Au/ZnO-NW/Au PRM cell clearly demonstrates the variations with temperature in the hysteretic $I-V$ switching characteristics (Fig. 6.4(a)). The threshold turn-on voltage for the reversely biased Schottky barrier of the PRM cell increased almost linearly with decreasing temperature (Fig. 6.4(b)), and the hysteresis loop increased with the decreasing temperature (Fig. 6.4(a)). The magnitudes of the current for PRM cell at

Fig. 6.3 $I-V$ characteristics
of ZnO PRM cells after 30,
20, and 10 minutes of oxygen
plasma treatment [17]
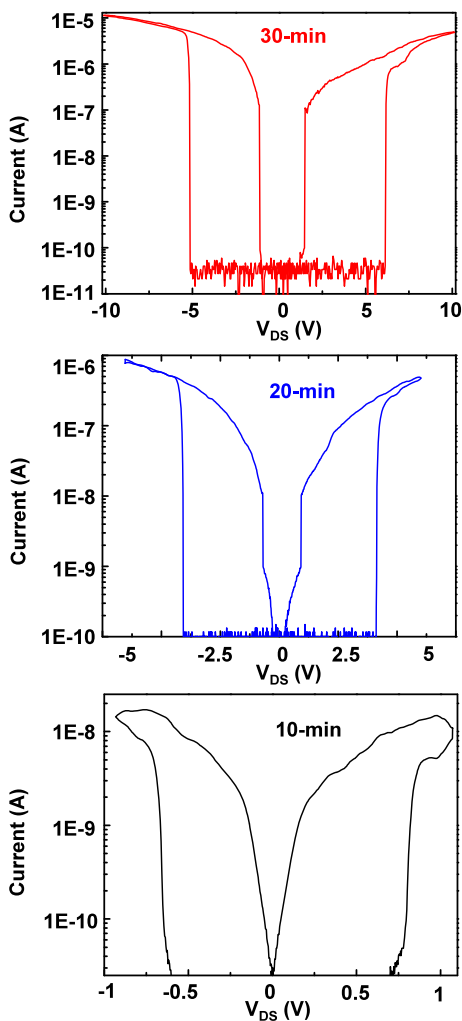
very large bias ($V = \pm 10$ V) were almost constant and independent of temperature
(Fig. 6.4(a)).

Although the nature of resistive switching and related charge transport process
at microscale in M–S–M structures is still under debate [1–5], the movement of
charged species that modulates the current flow seems to be a dominant mecha-
nism [3]. Drift/diffusion of defects such as positively charged oxygen vacancies
under applied electrical field has been suggested to change the electronic barrier at
the metal/semiconductor interface, which possibly results in the observed resistive
switching [4]. Oxygen vacancies are known to belong to the predominant ionic de-
fects in ZnO [26] and can influence the Schottky contacts between ZnO and metal
electrodes [24]. On the basis of the experimental results, a general model based
on the coupled transport of charged dopants and electrons under applied electric
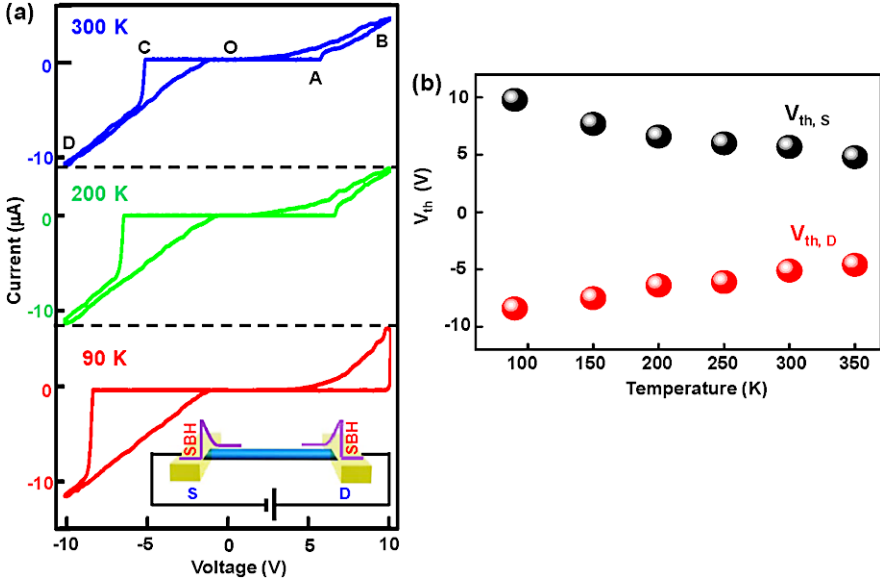
Fig. 6.4 Temperature-dependent I–V measurements of PRM cells at strain-free condition. (**a**) I–V characteristics of ZnO PRM cells at 300, 200, and 90 K, respectively. The sweeping frequency is 0.1 Hz. *Inset*: schematic showing the bias condition of the PRM cell when Schottky barrier at source side is reversely biased. (**b**) Dependence of threshold voltages on temperature. Both $V_{th,S}$ (in *black*) and $V_{th,D}$ (in *red*) increased in magnitudes almost linearly with the decreasing temperature. The hysteresis loop increased with the decreasing temperature [17]

field [4] is adopted and modified to explain the hysteretic switching behavior of the PRM cell without external deformation applied. The drift/diffusion of the oxygen vacancies towards the interface effectively reduces the local SBH, while the drift/diffusion of vacancies away from the interface increases the SBH.

The hysteretic switching sequences obtained at different temperatures can be characterized by four typical regions: (1) O–A, (2) A–B–O, (3) O–C, and (4) C–D–O, as labeled in Fig. 6.4(a) as an example. For easy discussion, the bias is set to be applied on the drain (D) electrode with respect to the source (S) side (Inset sketch in Fig. 6.4(a)). The overall macroscopic resistance of the PRM cell is $R_{PRM} = R_S + R_{NW} + R_D$, where R_S and R_D are the electrical resistances contributed by Schottky barriers at source and drain sides that may vary during the experiment and R_{NW} is the intrinsic resistance of the ZnO NW. It has previously been demonstrated that for semiconductor NW-based M–S–M structure, the I–V transport characteristic is normally dictated by the reversely biased Schottky barrier side [19, 27, 28]. As the bias voltage sweeps from O to A with the drain side forward-biased, the voltage drops mainly at the reversely biased source side. The total resistance of PRM cell is $R_{PRM} \sim R_S$ (with $R_S \gg R_{NW}, R_D$), which is the HRS state. The lower voltage at the source side attracts oxygen vacancies towards the interface to modify the contact barrier at the source. The switching from HRS to LRS state occurs at a larger bias beyond point A, in corresponding to a largely reduced

Fig. 6.5 $I-V$ characteristic for PRM cell in region O–B and D–O in Fig. 6.4. The numerical fitting curves show that $\ln(I)$ linearly depends on $V^{1/4}$, which indicates that thermionic emission-diffusion dominates the transport at the reverse-biased barriers
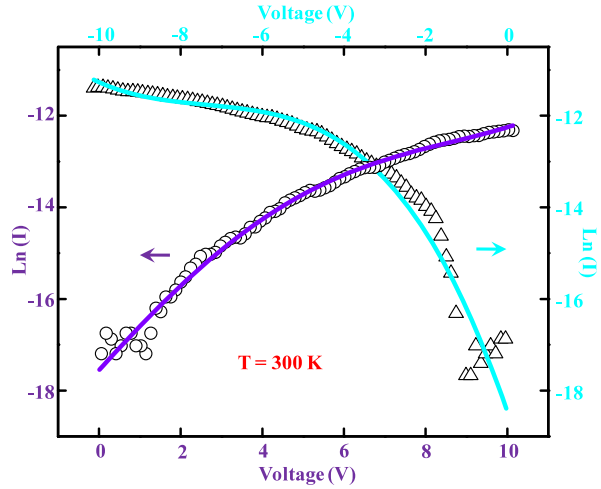

SBH at the source side. When the bias voltage sweeps from point A to point O through point B, the $\ln(I)-V$ curve for region B–O (empty circle in Fig. 6.5) shows that $\ln(I)$ relates to $V^{1/4}$, as confirmed by the numerical fitting curve (purple line in Fig. 6.5). This indicates that the thermionic emission-diffusion model dominates the transport at the reverse-biased source barrier [29]. An accelerated diffusion of the oxygen vacancies toward the source side at a large applied voltage and their accumulation are considered as the cause of the hysteresis observed in $I-V$ curve.

As the applied bias switches the polarity from point O to point C, the source side is now forward-biased and the bias voltage drops mainly at the reversely biased drain side with the total resistance of PRM cell $R_{PRM} \sim R_D$, which is the new HRS state. Oxygen vacancies near the drain side are attracted towards and accumulated at the reversely biased drain barrier to modify the interface contact, while oxygen vacancies previously piled up at the source side are drifting away. Similar to the case in region O–A, the switch from HRS to LRS state occurs only after a larger bias beyond point C is applied. When the bias voltage sweeps from point C to point O through point D, the $\ln(I)-V$ curve for region D–O (empty triangle in Fig. 6.5) can again be numerically fitted using the $\ln(I) \sim V^{1/4}$ relationship (blue line in Fig. 6.5), indicating that the thermionic emission-diffusion model also dominates the transport at the reverse-biased drain barrier.

It can also be observed that both $V_{th,S}$ and $V_{th,D}$ and hence the width of the HRS window increased as the temperature decreased from 350 to 90 K (Fig. 6.4(b)). Qualitatively, this can be understood since the drift/diffusion of the charged ions/dopants and electrons are thermally activated processes. Employing the rigid point ion model derived by Mott and Gurney [30], the diffusion coefficient of oxygen vacancy is given by $D = D_0 \cdot \exp(-E_a/kT)$ and the drift velocity is $v = a \cdot f \cdot \exp(-E_a/kT) \cdot \sinh(qE_a/2kT)$, where E_a is the activation energy, k is the Boltzmann constant, a is the effective hopping distance for the ion to hop between potential wells, f is the attempt-to-escape frequency. At decreased temperatures, larger bias is required to attract sufficient oxygen vacancies towards the
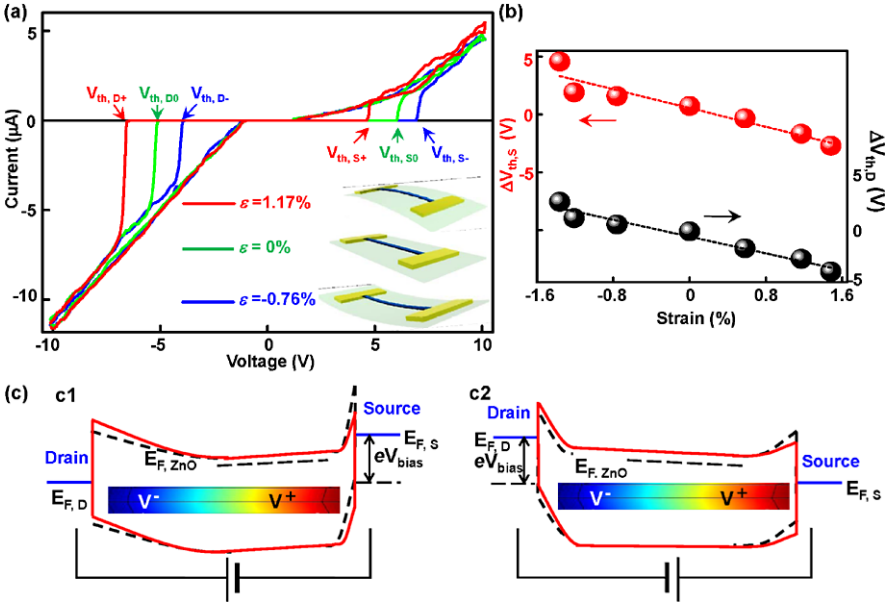
Fig. 6.6 Stain-modulated hysteretic switching of PRM cell. (**a**) $I-V$ characteristics of ZnO PRM cells under tensile, zero and compressive strains, respectively. (**b**) Dependence of threshold voltages on applied strains. Both $V_{th,S}$ (in *red*) and $V_{th,D}$ (in *black*) almost linearly depends on strain applied to the PRM cell, while the width of the HRS window remains almost constant for different strain values. (**c**) Schematic of band-diagram of PRM cell under tensile strain. (**c1**) Schottky barrier at drain side is forward-biased. (**c2**) Schottky barrier at drain side is reversely biased. *Red solid lines* represent band-diagrams after tensile strain is applied. *Black dashed lines* represent band-diagrams under strain-free condition. The color gradient represents the distribution of piezopotential field [17]

respective reversely biased barrier to switch the PRM cell from HRS to LRS state within the timescale in the experimental setup (the sweeping frequency of the bias signal was 0.1 Hz).

6.4 Piezotronic Effect on Electromechanical Memory

The external mechanical perturbation induced strain (ε_g) acts as the programming input for modulating the hysteretic $I-V$ characteristics of the PRM cell. A positive/negative strain is created when the ZnO NW is stretched/compressed (see Supporting Information for calculation of the strain in the PRM cell). Interesting phenomena were observed when a PRM cell experienced straining (Fig. 6.6(a)). When the PRM cell was tensile stretched ($\varepsilon = 1.17$ %), the hysteretic switching curve shifted towards lower voltage side by 1.49 V (red line in Fig. 6.6(a)); when the cell was compressively deformed ($\varepsilon = -0.76$ %), the hysteretic switching curve shifted towards higher voltage side by 1.18 V (blue line in Fig. 6.4(a)). $V_{th,S+}$,

Fig. 6.7 Ratio of conductance at LRS and HRS for the PRM cell under different strains. The ratio of conductance at LRS and HRS remains steady at high values ($\sim 10^5$) under different strains, demonstrating the stable performance of the PRM cell [17]
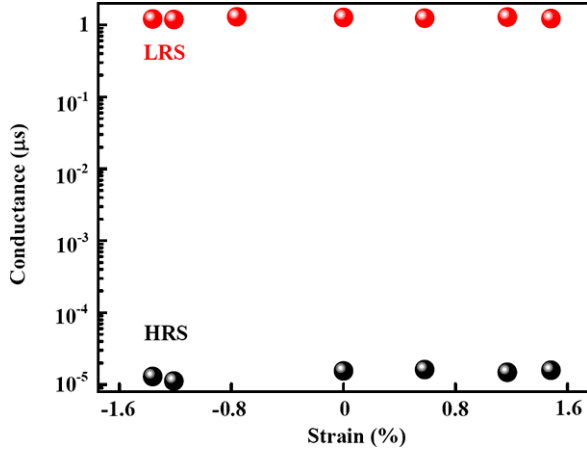
$V_{\text{th,S0}}$, $V_{\text{th,S}-}$, and $V_{\text{th,D}+}$, $V_{\text{th,D0}}$, $V_{\text{th,D}-}$ are the threshold switching voltages for the PRM cell with tensile, zero and compressive strains, respectively. The same hysteretic switching curves can then be plotted in a semi-logarithmic current scale to illustrate and highlight the characteristics of the curves (Fig. 6.8). The ratios of conductance between LRS and HRS for the PRM cell remain steady at high values ($\sim 10^5$) under different strains (Fig. 6.7), demonstrating the stable performance of the cell and its potential feasibility for applications in flexible memory and logic operations [19]. The intrinsic rectifying behavior of the PRM cell may solve the sneak path problem as well as reduce the static power consumption [23], which allows for construction of large passive resistive-switching device arrays. The changes in threshold switching voltages of the PRM cell with different strains have been plotted in Fig. 6.6(b). It can be seen that the change in both $V_{\text{th,S}}$ and $V_{\text{th,D}}$ almost linearly depends on strain applied to the PRM cell, while the width of the HRS window ($V_{\text{th,S}i} - V_{\text{th,D}i}$, where $i = +, 0, -$) remains almost constant for different strain values. This strain-modulated change in the threshold switching voltages was also observed for other PRM cells with oxygen–plasma treatment.

It is well known that ionic polarization in ZnO can be induced by strain owing to the lacking of center symmetry in ZnO, which can strongly affect the charge transport [18]. Novel effects [31] and applications [17, 27, 32] have been observed and implemented utilizing the piezotronic effect in ZnO [18]. The fundamental concept of the piezotronic effect is that the SBH at the metal–semiconductor contact can be effectively tuned by the strain-induced piezoelectric polarization charges at the interface. The local conduction band profile can then be modified by shifting the local Fermi level. The change in SBH induced by piezoelectric polarization is given approximately by $\Delta \phi_B = \sigma_{\text{pol}} \cdot D^{-1} \cdot (1 + 1/(2q_s w_d))^{-1}$, where σ_{pol} is the volume density of the polarization charge and directly related to the piezoelectric polarization P vector, D is the two-dimensional density of interface states at the Fermi level at the Schottky barrier, q_s is the two-dimensional screening parameter, and w_d is the width of the depletion layer [33]. Thus the mechanical strain can effectively change the local contact characteristics as well as the charge carrier
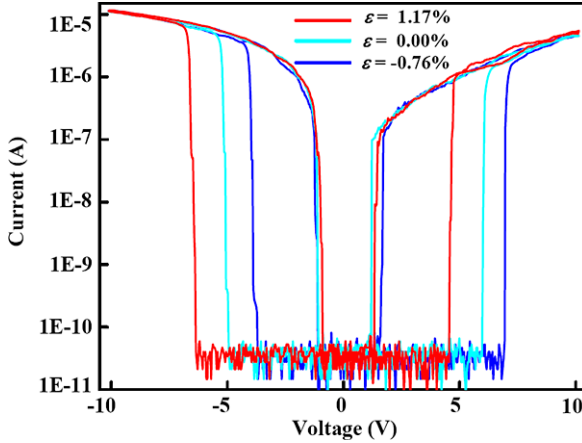
Fig. 6.8 Stain-modulated hysteretic switching curves of PRM cell in a semi-logarithmic current scale. The upper and lower branches of the hysteretic $I-V$ characteristics correspond to the LRS and HRS states for PRM cell with different strains. Abrupt transitions between LRS and HRS branches of the hysteretic $I-V$ curves occur at the respective threshold switching voltages, which are indicated by series of lines between the LRS and HRS branches

transport process. Based on the above discussions, the modulation effect of strain on the hysteretic switching behavior of the PRM cell, as shown in Figs. 6.6(a)–(b), can then be understood and explained using the band-diagram of the working device (Fig. 6.6(c)). If the PRM cell is under tensile strain with the Schottky barrier at drain side being forward-biased ($V > 0$ in Fig. 6.6(a)), the positive piezoelectric potential resulting from the positive strain-induced polarization charges reduced the SBH at the reverse-biased source barrier, while the negative piezoelectric potential resulting from the negative strain-induced polarization charges increased the SBH at the forward-biased drain barrier (red line in Fig. 6.6(c1)). Since the $I-V$ characteristic in this situation is dictated by the reversely biased source barrier, the existence of strain-induced piezoelectric potential results in the shift of switching threshold voltage from $V_{th,S0}$ to $V_{th,S+}$, indicating only a smaller bias is required to switch the PRM cell from HRS to LRS state. Alternatively, if the Schottky barrier at drain side is reverse-biased ($V < 0$ in Fig. 6.6(a)), the SBH is still reduced at the source barrier while it is increased at the drain barrier (Fig. 6.6(b2)) since the polarity of the strain did not change, and hence the piezoelectric potential remained negative and positive at source and drain barriers, respectively. The $I-V$ characteristic is now dictated by the reversely biased drain side in this case, and a shift of switching threshold voltage from $V_{th,D0}$ to $V_{th,D+}$ was observed, indicating that a larger bias has to be applied in order to switch the PRM cell from HRS to LRS state. By the same token, in the case of applying a compressive strain to the PRM cell, the shift of switching threshold voltage from $V_{th,S0}$ to $V_{th,S}$ and $V_{th,D0}$ to $V_{th,D}$ can be explained.

Under the strain-free condition and if the applied external bias exceeds the threshold voltage, the device is in LRS, and the concentration of oxygen vacancies in the

NW can significantly influence the total conductance of the NW as well as the SBHs at the source/drain (see Figs. 6.1(a1)–(a3) and 6.2). Now we consider the case that a strain is applied to the PRM cell. The effect of the piezopotential can be equivalently taken as applying a positive voltage at the barrier interface if the local piezoelectric polarization charges are positive, which in effect decreases the value of the external bias required to overcome the SBH at the interface. Alternatively, a negative voltage is created to act on the interface if the polarization charges are negative, which increases the value of the external bias required to overcome the barrier at the interface. From the data shown in Fig. 6.6, the HRS window remains almost constant regardless of the magnitude and sign of the applied strain, indicating that the shifts in the observed threshold voltages under different strains are dictated by the piezoelectric polarization charges at the interfaces and the contribution from the diffusion of the oxygen vacancies has negligible effect. This is because the oxygen vacancies are distributed in the entire NW, while the piezoelectric charges are accumulated right at the very near barrier interface in a region of less than a sub-nanometer. The diffusion force contributed by the piezoelectric charges on the oxygen vacancies is a long-range interaction force, thus the variation of the vacancy concentration at the interface owing to piezoelectric effect is rather small. Furthermore, the entire I–V curves are "translated" for a constant voltage, that is, the change of threshold switch voltage caused by the piezoelectric charges. For the samples pre-treated in oxygen plasma, the concentration of the oxygen vacancies was largely reduced in the NW, thus, the screening effect of the free charge carriers to the piezoelectric charges was significantly reduced, and the effect of the piezoelectric charges is enhanced [34]. Therefore, the shifts in threshold switch voltages due to piezoelectric polarization at both drain and source sides for a fixed strain have the same magnitude but opposite polarities, provided that the doping level is low. This indicates that the magnitude of the piezopotential at the interface is as large as 1.2 V at $0.5 \sim 0.76$ % of strain. The oxygen–plasma pre-treatment to the ZnO NWs may also improve the output of the nanogenerator [34].

6.5 Rewritable Electromechanical Memory

The fabricated PRM can function as an electromechanical memory, in which the write/read access can be programmed via mechanical actuation. A pulse train consisting of several write/read/erase pulses is applied to the PRM cell to record and read out the polarity/logic levels of the "stored" strain in the cell, by monitoring the characteristic patterns in the output current (Fig. 6.9). The data shown in Fig. 6.9 were obtained for the same PRM cell under different strain status, which is equivalent to the cases of three identical PRM cells under tensile strain (A cell), zero strain (B cell) and compressive strain (C cell), for easy description. First, a positive write pulse (10 ms) with $V_{th,S0} < V_{write1} < V_{th,S}$ is applied to these three cells. This short pulse sets the A and B cells to switch from the HRS to the LRS state, while the C cell remains in the HRS state. The status of the three cells is then read out by a read
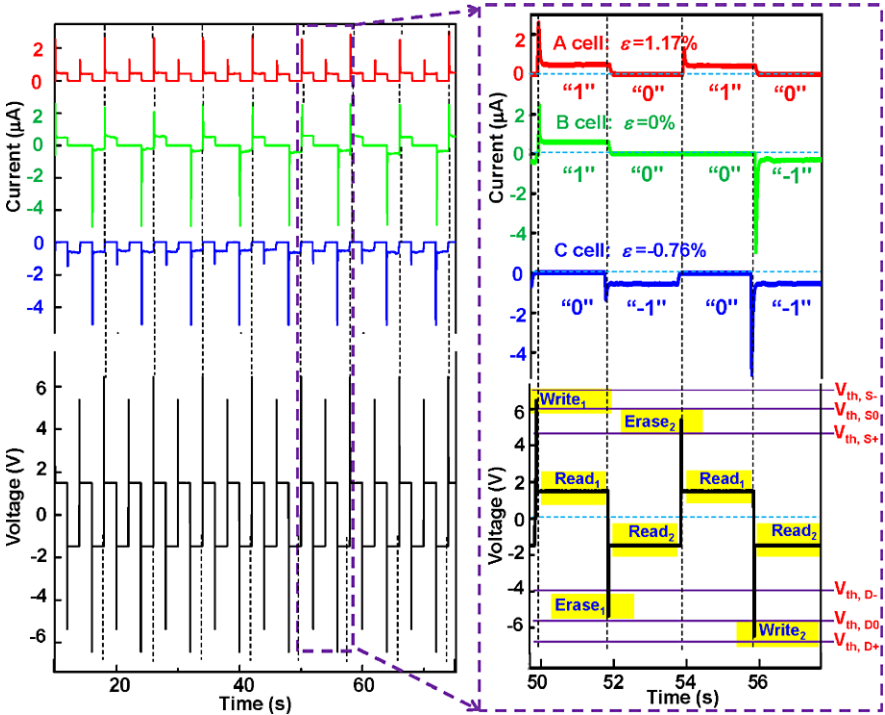
Fig. 6.9 Write/read access of PRM cell as an electromechanical memory. A pulse train consisting of several write/read/erase pulses was applied to the PRM cell to record and read out the logic levels of the "stored" strain in the cell. Each write/erase pulse was followed by a read pulse with positive or negative polarity, respectively. The following voltage amplitudes were applied: 6.44 V (write 1), 1.5 V (read 1), -5.35 V (erase 1), -1.5 V (read 2), 5.37 V (erase 2) and -6.42 V (write 2). Short current spikes occur in the output reading current with the write/erase pulses, if the resistance states (HRS to LRS) change in the PRM cell [17]

pulse (2 s) with a small magnitude ($V_{\text{read1}} < V_{\text{th,S+}}$). Subsequently, a negative erase pulse (10 ms) with $V_{\text{th,D0}} < V_{\text{erase1}} < V_{\text{th,D}}$ resets the A and B cells from the LRS to the HRS state, while it sets the C cell into the LRS state. A follow-up read pulse (2 s) with a small negative value ($V_{\text{read1}} > V_{\text{th,D}}$) is applied to read the new states of the cells. In the third step, a positive erase pulse (10 ms) with $V_{\text{th,S+}} < V_{\text{erase2}} < V_{\text{th,S0}}$ sets the A cell from the HRS to the LRS state again, while it keeps the B and C cells in the HRS state. The same V_{read1} pulse is then applied to read the new states of the cells. Finally, a negative write pulse (10 ms) with $V_{\text{th,D+}} < V_{\text{write2}} < V_{\text{th,D0}}$ resets the A cell into the HRS state, while it sets the B and C cells into the LRS state. The same V_{read2} pulse is then applied to read the new states of the cells. After the above series of the pulse train is applied, the waveform of the output currents of the cells is monitored and analyzed (Fig. 6.9). If the logic levels of the output currents with positive, almost zero and negative values are labeled as "1", "0" and "-1", the logic pattern of "1 0 1 0" indicates the positive nature of the "stored" strain in A cell. The

logic patterns of "1 0 0 −1" and "0 −1 0 −1" represent the zero and negative strain status of the B and C cells, respectively. A quantitative analysis of the magnitudes of the output currents can give the absolute values of the strains stored in the PRM cells. Although there have been numerous research and commercial products on strain detection and measurements such as semiconductor MEMS/NEMS piezoresistive strain gauges [35, 36], the PRM cells demonstrated here are fundamentally different from the these devices. Piezoresistance effect is a non-polar and symmetric effect resulting from the band structure change, while the PRM cells are based on the asymmetric piezotronic effect. ZnO is a polar structure along c-axis, straining in axial direction (c-axis) creates a polarization of cations and anions in the NW growth direction, resulting in a piezopotential drop from V^+ to V^- along the NW, which produces an asymmetric effect on the changes in the Schottky barrier heights (SBHs) at the drain and source electrodes. The strain sensor based on the piezotronic effect has been reported to possess much higher sensitivity than previously reported devices [27].

6.6 Summary

By utilizing the strain-induced polarization charges created at the semiconductor/metal interface under externally applied deformation as a result of the piezotronic effect, the switching characteristics of the ZnO NW resistive switching devices can be modulated and controlled. We further demonstrated that the logic levels of the strain applied on the memory cell can be recorded and read out for the first time utilizing the piezotronic effect [17, 18], which has the potential for implementing novel nanoelectromechanical memories and integrating with NEMS technology to achieve micro/nanosystems capable of intelligent and self-sufficient multidimensional operations [18, 20]. Taking advantage of the recently developed large-scale fabrication technique of ZnO NW arrays [37], non-volatile resistive switching memories using ZnO NW array as the storage medium may be readily engineered and implemented for applications such in flexible electronics and force/pressure imaging. Non-Boolean neuromorphic computing might also be realized by integrating arrays of high-density resistive memory cells [38, 39] on flexible substrates.

References

1. R. Waser, M. Aono, Nanoionics-based resistive switching memories. Nat. Mater. **6**(11), 833–840 (2007)
2. A. Sawa, Resistive switching in transition metal oxides. Mater. Today **11**(6), 28–36 (2008)
3. D.B. Strukov, G.S. Snider, D.R. Stewart, R.S. Williams, The missing memristor found. Nature **453**(7191), 80–83 (2008)
4. J.J. Yang, M.D. Pickett, X.M. Li, D.A.A. Ohlberg, D.R. Stewart, R.S. Williams, Memristive switching mechanism for metal/oxide/metal nanodevices. Nat. Nanotechnol. **3**(7), 429–433 (2008)

5. B.J. Choi, D.S. Jeong, S.K. Kim, C. Rohde, S. Choi, J.H. Oh, H.J. Kim, C.S. Hwang, K. Szot, R. Waser, B. Reichenberg, S. Tiedke, Resistive switching mechanism of TiO_2 thin films grown by atomic-layer deposition. J. Appl. Phys. **98**(3), 033715 (2005)

6. S.H. Jo, K.H. Kim, W. Lu, High-density crossbar arrays based on a Si memristive system. Nano Lett. **9**(2), 870–874 (2009)

7. D.B. Strukov, K.K. Likharev, Prospects for terabit-scale nanoelectronic memories. Nanotechnology **16**(1), 137–148 (2005)

8. Q.F. Xia, W. Robinett, M.W. Cumbie, N. Banerjee, T.J. Cardinali, J.J. Yang, W. Wu, X.M. Li, W.M. Tong, D.B. Strukov, G.S. Snider, G. Medeiros-Ribeiro, R.S. Williams, Memristor—CMOS hybrid integrated circuits for reconfigurable logic. Nano Lett. **9**(10), 3640–3645 (2009)

9. J. Borghetti, G.S. Snider, P.J. Kuekes, J.J. Yang, D.R. Stewart, R.S. Williams, 'Memristive' switches enable 'stateful' logic operations via material implication. Nature **464**(7290), 873–876 (2010)

10. R. Waser, R. Dittmann, G. Staikov, K. Szot, Redox-based resistive switching memories—nanoionic mechanisms, prospects, and challenges. Adv. Mater. **21**(25–26), 2632–2663 (2009)

11. D.H. Kwon, K.M. Kim, J.H. Jang, J.M. Jeon, M.H. Lee, G.H. Kim, X.S. Li, G.S. Park, B. Lee, S. Han, M. Kim, C.S. Hwang, Atomic structure of conducting nanofilaments in TiO_2 resistive switching memory. Nat. Nanotechnol. **5**(2), 148–153 (2010)

12. J. Chen, W. Wang, M.A. Reed, A.M. Rawlett, D.W. Price, J.M. Tour, Room-temperature negative differential resistance in nanoscale molecular junctions. Appl. Phys. Lett. **77**(8), 1224–1226 (2000)

13. A. Baikalov, Y.Q. Wang, B. Shen, B. Lorenz, S. Tsui, Y.Y. Sun, Y.Y. Xue, C.W. Chu, Field-driven hysteretic and reversible resistive switch at the $AgPr_{0.7}Ca_{0.3}MnO_3$ interface. Appl. Phys. Lett. **83**(5), 957–959 (2003)

14. Y.J. Dong, G.H. Yu, M.C. McAlpine, W. Lu, C.M. Lieber, Si/a-Si core/shell nanowires as nonvolatile crossbar switches. Nano Lett. **8**(2), 386–391 (2008)

15. S. Seo, M.J. Lee, D.H. Seo, E.J. Jeoung, D.S. Suh, Y.S. Joung, I.K. Yoo, I.R. Hwang, S.H. Kim, I.S. Byun, J.S. Kim, J.S. Choi, B.H. Park, Reproducible resistance switching in polycrystalline NiO films. Appl. Phys. Lett. **85**(23), 5655–5657 (2004)

16. K. Szot, W. Speier, G. Bihlmayer, R. Waser, Switching the electrical resistance of individual dislocations in single-crystalline $SrTiO_3$. Nat. Mater. **5**(4), 312–320 (2006)

17. Z.L. Wang, Piezopotential gated nanowire devices: piezotronics and piezo-phototronics. Nano Today **5**, 540–552 (2010)

18. W.Z. Wu, Z.L. Wang, Piezotronic nanowire-based resistive switches as programmable electromechanical memories. Nano Lett. **11**(7), 2779–2785 (2011)

19. Z.W. Pan, Z.R. Dai, Z.L. Wang, Nanobelts of semiconducting oxides. Science **291**, 1947–1949 (2001)

20. Z.L. Wang, Toward self-powered sensor networks. Nano Today **5**(6), 512–514 (2010)

21. W.Z. Wu, Y.G. Wei, Z.L. Wang, Strain-gated piezotronic logic nanodevices. Adv. Mater. **22**(42), 4711–4715 (2010)

22. J.C. Scott, Is there an immortal memory? Science **304**(5667), 62–63 (2004)

23. E. Linn, R. Rosezin, C. Kugeler, R. Waser, Complementary resistive switches for passive nanocrossbar memories. Nat. Mater. **9**(5), 403–406 (2010)

24. M.W. Allen, S.M. Durbin, Influence of oxygen vacancies on Schottky contacts to ZnO. Appl. Phys. Lett. **92**(12), 12210 (2008)

25. E.H. Rhoderick, R.H. Williams, *Metal–Semiconductor Contacts* (Clarendon, Oxford, 1988)

26. L. Schmidt-Mendem, J.L. MacManus-Driscoll, ZnO-nanostructures, defects, and devices. Mater. Today **10**(5), 40–48 (2007)

27. J. Zhou, P. Fei, Y.D. Gu, W.J. Mai, Y.F. Gao, R.S. Yang, G. Bao, Z.L. Wang, Piezoelectric-potential-controlled polarity-reversible Schottky diodes and switches of ZnO wires. Nano Lett. **8**(11), 3973–3977 (2008)

28. Z.Y. Zhang, K. Yao, Y. Liu, C.H. Jin, X.L. Liang, Q. Chen, L.M. Peng, Quantitative analysis of current–voltage characteristics of semiconducting nanowires: decoupling of contact effects.

Adv. Funct. Mater. **17**(14), 2478–2489 (2007)
29. S.M. Sze, *Physics of Semiconductor Devices* (Wiley, New York, 1981)
30. N.F. Mott, R.W. Gurney, *Electronic Processes in Ionic Crystals*, 2nd edn. (Clarendon, Oxford, 1948)
31. K.W. Chung, Z. Wang, J.C. Costa, F. Williamsion, P.P. Ruden, M.I. Nathan, Barrier height change in GaAs Schottky diodes induced by piezoelectric effect. Appl. Phys. Lett. **59**(10), 1191 (1991)
32. W.H. Liu, M.B. Lee, L. Ding, J. Liu, Z.L. Wang, Piezopotential gated nanowire–nanotube hybrid field-effect transistor. Nano Lett. **10**(8), 3084–3089 (2010)
33. Y. Zhang, Y.F. Hu, S. Xiang, Z.L. Wang, Effects of piezopotential spatial distribution on local contact dictated transport property of ZnO micro/nanowires. Appl. Phys. Lett. **97**(3), 033509 (2010)
34. Y.F. Gao, Z.L. Wang, Equilibrium potential of free charge carriers in a bent piezoelectric semiconductive nanowire. Nano Lett. **9**(3), 1103–1110 (2009)
35. L. Cao, T.S. Kim, S.C. Mantell, D.L. Polla, Simulation and fabrication of piezoresistive membrane type MEMS strain sensors. Sens. Actuators A, Phys. **80**(3), 273–279 (2000)
36. E. Mile, G. Jourdan, L. Duraffourg, S. Labarthe, C. Marcoux, D. Mercier, P. Robert, P. Andreucci, Sensitive in plane motion detection of NEMS through semiconducting (p+) piezoresistive gauge transducers. IEEE Sens. J. **1**(3), 1286–1289 (2009)
37. Y.G. Wei, W.Z. Wu, R. Guo, D.J. Yuan, S.M. Das, Z.L. Wang, Wafer-scale high-throughput ordered growth of vertically aligned ZnO nanowire arrays. Nano Lett. **10**(9), 3414–3419 (2010)
38. K. Boahen, Neuromorphic microchips. Sci. Am. **292**(5), 56–63 (2005)
39. S.H. Jo, T. Chang, I. Ebong, B.B. Bhadviya, P. Mazumder, W. Lu, Nanoscale memristor device as synapse in neuromorphic systems. Nano Lett. **10**(4), 1297–1301 (2010)